



**HAL**  
open science

# Prestress state evolution during thermal activation of memory effect in concrete beams strengthened with external SMA wires

A. Debska, Piotr Gwoździewicz, A. Seruga, Xavier Balandraud, J. F Destrebecq

## ► To cite this version:

A. Debska, Piotr Gwoździewicz, A. Seruga, Xavier Balandraud, J. F Destrebecq. Prestress state evolution during thermal activation of memory effect in concrete beams strengthened with external SMA wires. Archives of civil and mechanical engineering, 2020, 20 (4), 10.1007/s43452-020-00133-y . hal-03039225

**HAL Id: hal-03039225**

**<https://uca.hal.science/hal-03039225>**

Submitted on 3 Dec 2020

**HAL** is a multi-disciplinary open access archive for the deposit and dissemination of scientific research documents, whether they are published or not. The documents may come from teaching and research institutions in France or abroad, or from public or private research centers.

L'archive ouverte pluridisciplinaire **HAL**, est destinée au dépôt et à la diffusion de documents scientifiques de niveau recherche, publiés ou non, émanant des établissements d'enseignement et de recherche français ou étrangers, des laboratoires publics ou privés.



Distributed under a Creative Commons Attribution 4.0 International License

# **Prestress state evolution during thermal activation of memory effect in concrete beams strengthened with external SMA wires**

A. Debska<sup>1</sup>, P. Gwozdziwicz<sup>2</sup>, A. Seruga<sup>2</sup>, X. Balandraud<sup>3</sup>, J.F. Destrebecq<sup>3</sup>

<sup>1</sup> Aldebud Aleksandra Dębska, 30689 Kraków, Poland

<sup>2</sup> Cracow University of Technology, 31155 Kraków, Poland

<sup>3</sup> Université Clermont Auvergne, CNRS, SIGMA Clermont, Institut Pascal, F-63000 Clermont-Ferrand, France

Corresponding author: Piotr Gwoździwicz (Tel.: +48126282311, email: [pgwozdziwicz@pk.edu.pl](mailto:pgwozdziwicz@pk.edu.pl))

**Abstract:** The memory effect of shape-memory alloys (SMAs) has opened interesting perspectives to create prestress states in concrete elements. However, the procedure has not been yet fully resolved due to the complex thermomechanical behavior of these alloys, in addition to the practical difficulties of mechanical coupling between SMA and concrete elements. The present study deals with tests on the development of prestressing forces in concrete beams during the thermal cycle required in the procedure. Pre-stretched nickel-titanium wires were externally placed on concrete prismatic beams equipped with strain gauges. As concrete rupture may occur during the heating by the Joule effect, a compromise must be found between the SMA pre-stretch level and the maximum temperature to be applied before returning to ambient temperature. A macroscopic model was developed to analyze this compromise. The complex thermomechanical response of SMAs implies a particular attention in the definition of the ambient temperature and heating conditions for the creation of prestress states in concrete components.

**Keywords:** shape memory alloy; prestressing force; bending; civil engineering; transformation temperature; nickel-titanium

# 1. Introduction

Shape memory alloys (SMAs) are active materials that have the ability to cancel apparent “plastic” strain by heating, a phenomenon known as the *memory effect* [1-5]. When the latter is mechanically hindered, the SMA component therefore develops forces, a mechanism that has found many applications in engineering. The underlying physical phenomenon is a solid-solid transition between two phases, namely *austenite* (A) and *martensite* (M), triggered by temperature and stress. Roughly, austenite and martensite are present at “high” and “low” temperatures respectively. In the austenite state, a SMA component has a unique memorized shape that was defined during material elaboration. Note that SMAs are mainly supplied in the form of wires, springs, foils, sheets, bars and tubes. The A→M transformation can be achieved by cooling or deforming. In the martensite state, a SMA component can be “permanently” deformed by several percent. The recovery of the memorized shape is obtained by heating (activation of the M→A transformation). Note that the Joule effect is easy to use thanks to the metallic nature of SMAs, although heat loss may penalize the amplitude of the temperature increase [6]. The memory effect has opened interesting perspectives of applications in many engineering fields, in particular in civil engineering [7-16]. Almost twenty years ago, Mazzolani and Madara (2002) discussed the advantages of advanced metals including SMAs in the field of restoration of buildings, in particular of monumental buildings, in spite of their higher cost compared to structural mild steel [7]: suitability for strengthening problems, potentiality for transverse confinement of masonry walls and ability of energy dissipation for seismic protection devices. Song *et al.* (2005) reviewed applications of SMAs in control of civil engineering structures, both as damping elements and structural self-rehabilitation elements [8, 9]. Janke *et al.* (2005) presented overviews and limits of the applications in civil engineering, as well as new ideas in particular for the active confinement to create prestresses in concrete components [10]. Motavalli *et al.* (2008) discussed existing applications, laboratory tests and new concepts for energy dissipation devices and discussed the new generation of iron-based SMA as an alternative to high cost NiTi SMAs [12, 13]. Cladera *et al.* (2014) focused on the advantages of using iron-based SMAs for repairing existing structures and building new ones thanks to high recovery stresses (necessary for prestressing) and lower prices [14]. Dong *et al.* (2011) reviewed specific applications to bridge structures [15]. Recently, Casciati (2019) discussed

civil engineering applications particularly in terms of long-term performance in relation to fatigue resistance [16].

SMA offers interesting prospects for the creation of prestresses in concrete structures (beams and pylons). The long-term objective is to use these active materials on site avoiding the use of complex and cumbersome mechanical actuators while simplifying the implementation procedure. The issue of prestressing concrete elements with SMAs has not yet been fully resolved due to both the complex thermomechanical behavior of these alloys and the practical difficulties of transferring forces to the concrete elements. Literature shows applications to the strengthening of masonry structures and reinforced concrete (RC) structures, as well as to the reinforcement of concrete beams and columns. Zhao and Andrawes proposed in Ref. [17] the use of curved SMA wires to prestress a mortar plate connected with a concrete structure. The constructed connections allowed more than 80% of the recovery force to transfer to the concrete block for prestressing. Also, Shahverdi *et al.* developed in Ref. [18] a promising method to strengthen RC beams by embedding ribbed iron-based SMA bars in an additional shotcrete layer connected with the old concrete. Two RC beams were first prestressed using two and four SMA bars 8 mm in diameter, leading to about 300 MPa of recovery stresses in the bars. Afterwards, the strengthened beams were loaded until failure under four-point bending. Results showed a significantly higher cracking load level compared with un-strengthened beams: the loads in the strengthened beams were even 265% higher than that of un-strengthened beams. Rojob and El-Hacha investigated in Ref. [19] the long-term performance of RC beams strengthened with iron-based SMA bars under severe freeze-thaw cycles and sustained loading. The results revealed that the strengthened beams were better in flexural performance compared to the un-strengthened beams, with low degradation compared to other beams tested at room temperature. Miralami *et al.* studied in Ref. [20] the strengthening of circular RC column-foundation connections thanks to nickel-titanium SMA bars or the combination of SMA bars and carbon fiber reinforced polymer (CFRP) wraps. Columns were subjected to constant axial compressive loads and cyclic lateral displacements. Results showed that the strengthening SMA bars were able to reduce the residual deformation of the connections and that the combination of the SMA bars and CFRP wraps increased the ductility ratio parameter. Let us mention also research studies about anchorage systems of SMA components in construction elements, which are not standardized yet. Correct anchorage system is particularly important for civil engineering applications. According to Ref. [21], mechanical anchors are more favorable

compared for example with hook anchorage: the most practical and most cost effective method of anchoring SMA bars in concrete is based on screwlock mechanical anchors. A nail-anchor system was proposed in Ref. [22] as direct fastening technique for strengthening steel construction elements using iron-SMA strips; as indicated by the authors, the method is simple and reduces the time and cost of strengthening works.

The academic research on SMA reinforced concrete is currently very intense [23-26]. Many studies deal with the modification of the mechanical performances of concrete structures reinforced by SMAs. The present paper focuses on the creation of prestressing forces in SMA wires placed externally on concrete prismatic beams, prior to any external loading. It can be recalled that this mode of prestressing is difficult to manage because of the SMAs' complex behavior, which is triggered by the temperature and the stress while being strongly hysteretic [1-5]. The procedure requires pre-stretching of the SMA wires (to create martensite), placement of the wire on the beams, heating of the SMA wires by the Joule effect (to activate the  $M \rightarrow A$  transformation) and cooling down to ambient temperature. Our measurements concerned the development of the prestressing forces during the thermal cycle using strain gauges placed on the concrete beams. Our objective was *not* to analyze the mechanical properties of the reinforced beams, but to track the response of SMA wires during the thermal cycle required in the prestressing procedure. The paper is organized as follows. First, Section 2 concerns the thermomechanical properties of the SMA wires used to prestress the concrete beams. Section 3 is dedicated to the mechanical properties of the concrete used for the beams. Section 4 describes the experimental setup to monitor the prestressing process of the beams. Section 5 presents the results obtained from several configurations differing in terms of number, diameter and pre-stretch level of the SMA wires. Finally, Section 6 presents simulation results to analyze the mechanical coupling between the SMA wires and the concrete beam.

## **2. Thermomechanical properties of the SMA wires**

Experimental tests were carried out on nickel-titanium (NiTi) SMA wires supplied by Nimesis, Metz, France. Despite the higher cost of NiTi SMAs compared to copper-based and iron-based SMAs, this alloy was here selected because of its well-known stability over time,

both in terms of resistance to corrosion and to mechanical and thermal fatigue [27]. Wires were selected from the supplier's data sheets to be austenitic at positive room temperature (above 0°C). Three diameters were considered for the study: 1 mm, 2 mm and 3 mm. The wires were delivered in the form of coils 350 mm in diameter so that bending was limited during the transportation and storage of the wires. The study started with a characterization of the different wires before the tests on the concrete beams. Section 2.1 presents the measurement of the transformation temperatures. Section 2.2 is dedicated to a thermomechanical characterization of the wires.

## 2.1. Measurement of the transformation temperatures

Table 1 gives the values of the Austenite-start temperature ( $A_s$ ) for the three SMA alloys, determined by differential scanning calorimetry (DSC) by the supplier. The ASTM F2004 standard indicates that transformation temperatures derived from DSC may not agree with those obtained by other test methods due to the effects of strain and load on the transformation [28]. Dilatometry tests were thus also performed to measure the four transformation temperatures of the SMAs in stress-free state; namely Martensite-start ( $M_s$ ) and Martensite-finish ( $M_f$ ) for the  $A \rightarrow M$  transformation, and Austenite-start ( $A_s$ ) and Austenite-finish ( $A_f$ ) for the reverse transformation. A horizontal Netzsch DIL 402C dilatometer was employed using helium gas to eliminate potential effect of ambient atmosphere [29]. Small wire samples were prepared and measured at a room temperature of 25°C. Initial length  $L_0$  was nearly 5 mm for the 1 mm diameter wire, and nearly 15 mm for the 2 mm and 3 mm diameter wires. The following heating sequence was applied under small compression force (-0.3 N) at a temperature rate of  $\pm 10^\circ\text{C}/\text{min}$ :  $25^\circ\text{C} \rightarrow +100^\circ\text{C} \rightarrow -110^\circ\text{C} \rightarrow +100^\circ\text{C} \rightarrow -110^\circ\text{C} \rightarrow +40^\circ\text{C}$ . Figure 1 presents the relative variation in length *versus* temperature for the three wires. Classic thermal expansion and contraction are observed (linear variation of the sample's length with respect to the temperature):  $\sim 10 \times 10^{-6} \text{ K}^{-1}$  at high temperature (austenitic state) and  $\sim 7 \times 10^{-6} \text{ K}^{-1}$  at low temperature (martensitic state), see Table 1. These values are in agreement with the values of the literature for polycrystalline NiTi SMAs. Geometric “anomalies” are also visible. They can be attributed to a very small volume change between austenite and martensite and to the possible creation of so-called oriented martensite (*i.e.* deformed with respect to the austenite) upon cooling. Anyway, this enabled us to identify the beginning and end of the direct ( $A \rightarrow M$ ) and reverse ( $M \rightarrow A$ ) transitions. As

expected, the beginning and end of both transformations are not sharp, justifying the use of the tangent method: see intersections of the dashed blue lines. Temperature transformations  $M_s$ ,  $M_f$ ,  $A_s$  and  $A_f$  obtained by dilatometry are also listed in Table 1. A discrepancy in the  $A_s$  values is observed between the two measurement techniques. This could be due to the inherent uncertainty of the tangent method used for the two techniques which, moreover, are based on signals of different nature (namely heat flux for DSC and strain for dilatometry). As the beginnings and ends of phase change are relatively gradual, identification of the four transformation temperatures is actually sensitive and complex whatever the measurement technique. For our study, we considered the transformation temperatures determined by dilatometry. Indeed, our application is based on the deformation of SMA wires. It can be noted that  $M_s$  is lower than  $0^\circ\text{C}$  for the three wires, confirming that a full austenitic state is possible at positive room temperature. It is also noted that  $A_s$  is positive for the three wires. The fact that the ambient temperature  $T_{\text{amb}}$  is such that  $M_s < T_{\text{amb}} < A_s$  is interesting for the creation of residual prestresses (see Refs [30-34]), which gives here a small range of relevant ambient temperatures. The difference between  $A_s$  and  $M_s$  is equal  $21^\circ\text{C}$ ,  $11^\circ\text{C}$  and  $34^\circ\text{C}$  for the 1 mm, 2 mm and 3 mm diameter wires respectively (see dilatometry measurements in Table 1). These temperature amplitudes are small, especially for the 1 mm and 2 mm diameter wires, which limits their outdoor applications. Finding and using SMAs with higher differences between  $A_s$  and  $M_s$  is a next step of the present study. Finally, it is noted for the  $A_f$  values of the three types of wire can be exceeded by heating of a few tens of degrees, which allowed us to simply activate the memory effect thanks to the Joule effect. However, let us recall that the transformation temperatures increase with the stress (about 6–8 MPa per  $^\circ\text{C}$  for NiTi SMAs) [35].

## 2.2. Mechanical characterization

Mechanical tensile tests were performed on the SMA wires using a 20 kN Zwick 1455 uniaxial testing machine. A reference length of 120 mm was considered for the wire samples placed in the jaws of the machine. Due to practical constraints, ambient temperature  $T_{\text{amb}}$  was equal to  $15^\circ\text{C}$  for this characterization. Steps of the experimental procedure were as follows:

- heating of the wire in an oven at a temperature of  $+100^\circ\text{C}$  — As this temperature is higher than  $A_f$ , a full austenite state is obtained;

- natural return to ambient temperature — As  $T_{\text{amb}}$  is higher than  $M_s$ , the full austenite state is preserved;
- stretching at a displacement rate of 1.2 mm/min up to a maximum strain  $\epsilon_{\text{max}}$  set to 6% — This stretching yields an A $\rightarrow$ M transformation. The martensite created is classically named *twinned martensite* (to be opposed to the so-called *self-accommodating martensite* which is obtained by cooling in stress-free state and is not macroscopically deformed with respect to the austenite phase);
- unloading at a displacement rate of -1.2 mm/min — The obtained residual strain is referred to as  $\epsilon_{\text{res}}$  in the following;
- heating at “blocked” residual strain (*i.e.* overall strain kept at  $\epsilon_{\text{res}}$ ) for 120 s using the Joule effect — This heating yields a M $\rightarrow$ A transformation;
- and finally natural cooling to ambient temperature — The residual stress at the end of the procedure is referred to as  $\sigma_{\text{res}}$  in the following.

As an example, Fig. 2 shows the stress-strain curve obtained for the 3 mm diameter SMA wire, excluding the heating and cooling steps (see Fig. 3 for the thermal cycle). After elastic deformation of the austenite (Arrow 1), the A $\rightarrow$ M transformation occurred and it appears as a so-called stress plateau (Arrow 3). Note that the beginning of the transformation was accompanied by a stress drop (Arrow 2), usual for NiTi SMA alloys. The descending branch (Arrow 4) corresponds to the unloading of the sample. A residual strain  $\epsilon_{\text{res}} = 3.0\%$  is observed at the end of the unloading. It is due to the fact that martensite phase was partially kept upon unloading (nearly-elastic unloading). Figure 3 shows the time evolution of the tensile stress in the wire, including the heating and cooling at blocked residual strain. During heating (Arrow 5), the M $\rightarrow$ A transformation is accompanied by a sharp stress increase due to the memory effect in blocked strain condition. Let us note the slight stress increase during the cooling, due to the hindered thermal contraction (Arrow 6). A residual stress  $\sigma_{\text{res}}$  of 179 MPa was measured at the end of the procedure. Other parameters were identified from Fig. 2, namely the critical stress  $\sigma_{\text{cr}} = 340$  MPa of A $\rightarrow$ M transformation onset and the maximal stress  $\sigma_{\text{max}} = 349$  MPa during the stretching. Tests were also carried out the wires 1 mm and 2 mm in diameter: see results in Table 2. Note that apparent Young’s moduli may be identified from the initial slopes of the stress-strain curves. However, measuring the Young’s modulus of SMA materials remains delicate due to the difficulty in fixing SMA wires effectively at their ends. The superelasticity of the alloy makes clamping in the jaws of the

testing machine difficult. Moreover, the stress-induced austenite-to-martensite transition is accompanied by a decrease in wire cross-section, which can potentially lead to slippage in the clamping system. The apparent Young's modulus  $E_{app}$  was measured to about 35 GPa, 22 GPa and 16 GPa for the 1 mm, 2 mm and 3 mm diameter wires respectively. These values are much lower than the usual values for the austenite phase of NiTi SMAs (60-70 GPa [36]). Low values may be explained by the clamping's response, a slippage or the presence of residual martensite at the unloaded state. Anyway, it can be concluded that prestress states could be advantageously created by means of a thermal cycle if the SMA wires were fixed on concrete beams. In that case, the SMA strain would not be fully "blocked" because of the deformation of the concrete, penalizing the prestresses created. For the application to concrete beams presented in Section 4, the loading-unloading cycle of the SMA wires was preliminary performed on a home-made loading machine allowed to work at much lower temperature (around 0°C), enabling us to respect the condition  $M_s < T_{amb} \approx 0^\circ\text{C} < A_s$ .

### 3. Preparation and characterization of concrete elements

Twelve 40×100×500 mm<sup>3</sup> concrete beams were prepared to be equipped with the SMA wires. They were made from Portland cement CEM I 32.5 R and basalt aggregates from 2 mm to 8 mm. The composition per 1 m<sup>3</sup> was: cement 353.4 kg, basalt 1202.6 kg, river sand 560.0 kg, water 213.0 l and water-cement ratio of 0.6. Seven cube specimens (150×150×150 mm<sup>3</sup>) and six cylinder specimens (300 mm × ø 150 mm) were also prepared for characterization of concrete properties. All concrete elements were cast in steel forms. Seven days after concreting, they were removed from the forms and protected with foils for 28 days. Elements were weighted to measure the concrete density: mean value of 2465 kg/m<sup>3</sup> with coefficient of variation  $\nu$  equal to 1.1% were determined.

Compression tests were performed using EDU 400 compression tests apparatus. The mean compressive strength of the material was found at 51 MPa ( $\nu = 8.1\%$ ) for the cubes and 43 MPa ( $\nu = 8.1\%$ ) for the cylinders. Longitudinal strains were measured on the external surface of cylinders using four longitudinal DEMEC mechanical strain gauges, 150 mm in length. The value of the secant elasticity modulus at 0.4  $f_{c,cyl}$  was identified to  $E_c = 36.2$  GPa ( $\nu = 0.8\%$ ), where  $f_{c,cyl}$  is the ultimate compressive strength. In addition, two cylindrical

specimens were subjected to the loading procedure defined by the Building Research Institute (Instytut Techniki Budowlanej, ITB) in Warsaw, Poland [37]. Figure 4-a shows the applied stress level as a function of the longitudinal strain by  $0.1 f_{c,cyl}$  loading steps till failure. Figure 4-b shows the secant elastic modulus  $E_{cm}$  as a function of the loading level from  $0.2 f_{c,cyl}$  to  $0.6 f_{c,cyl}$ . Finally, split tensile strength tests were performed using ZD 40 testing machine. The tensile strength was determined to 4.4 MPa for the cylinders and 4.1 MPa for the cubes.

## 4. Experimental setup for the tests on concrete beams

Section 4.1 presents the experimental device for the tests on concrete beams equipped with the SMA wires. Section 4.2 presents the test conditions in terms of number and diameter of wires used for the tests.

### 4.1 Experimental device

Steel anchors were placed at the two ends of each concrete beam (see Fig. 5-a). Prior to the placement of the SMA wires, the latter were pre-stretched one by one using a specially designed tensile device (see Fig. 5-d). Note that all the operations on SMA wires were performed at an ambient temperature  $T_{amb}$  around  $0^{\circ}\text{C}$  (in practice between  $-1^{\circ}\text{C}$  and  $4^{\circ}\text{C}$ , see below). Steel plates were used to tight simultaneously all the pre-stretched SMA wires in the steel anchors, at a distance of 20 mm from the top surface of the beam (see Fig. 5-b). Rough surfaces were used to avoid slipping of the wires during the experiments. In details, the steps were:

- 1) “initialization” of SMA wires — Samples 500 mm in length were heated to about  $+100^{\circ}\text{C}$  and cooled down to ambient temperature, leading to a full austenitic state as explained in Section 2.2;
- 2) Pre-stretching of the SMA wires — The operation consisted in stretching up to a strain  $\varepsilon_{max}$  and unloading in order to obtain a residual strain as explained in Section 2.2;
- 3) Fixing of the pre-stretched SMA wires in the steel anchors at both ends of the concrete beam. No force was applied to the wires during their placement (in fact, they were simply straightened, with negligible tension force);

- 4) Connecting of the SMA wires to an adjustable electrical laboratory autotransformer (10A 220V/0-250V), see Fig. 5-c.

Several sensors were used for tracking the system response during the experiments (see Fig. 6):

- strain gauges – Electrofusion strain gauges 75 mm in length were installed in the longitudinal direction of the top and bottom surfaces of the concrete beams. A recording bridge HBM QuantumX MX840A, shielded cables and CatmanEasy-AP software were used for strain data acquisition. Note that a compensation system was employed using strain gauges installed on a reference concrete beam;
- temperature sensors – A temperature contact sensor was placed in contact with a SMA wire, while another one was placed as the surface of the concrete beam. A thermometer was also used to measure the ambient temperature;
- ammeter and voltmeter were used to measure the intensity and the voltage of the electric current in the SMA wires.

## 4.2 Test conditions

Table 3 shows the conditions of the first five tests performed on concrete beams equipped with SMA wires: number and diameter of the wires, maximum strain applied to pre-stretch the wires (designated  $\varepsilon_{\max}$  previously, see Fig. 2), ambient temperature  $T_{\text{amb}}$  and maximum temperature  $T_{\text{max}}$  of the SMA wires obtained by applying the Joule effect. It can be noted that the first test (#1) led to concrete beam failure during the heating stage: see Fig. 7. The excessive force level upon heating in that case resulted *a priori* from the too high pre-stretch level  $\varepsilon_{\max}$  (6%) and/or the too high maximum temperature  $T_{\text{max}}$ . The solution to avoid such ruptures is to define carefully the pre-stretching level and the maximum temperature for the SMA wires (see Section 6.3 about the compromise between these two parameters). The second test (#2) was done under the same conditions, but with a lower maximum temperature (45°C compared to 60°C): although the beam did not break, the appearance of micro-cracks could be assumed because the magnitude of prestressing was lower than expected (see section 5.3 below). It can be recalled that the transformation temperatures increase with the stress (about 6–8 MPa per °C for NiTi SMAs), making the choice of maximum temperature to be applied complicated. On the one hand, increasing the heating allows the M→A transformation

to progress (until potentially a total disappearance of the martensite phase). On the other hand, the more the martensite disappears, the more the stress in the SMA wires increases because the memory effect is hindered by the concrete beam to which they are attached. It was therefore decided to decrease the pre-stretch level  $\varepsilon_{\max}$  to 3% (roughly half as much twinned martensite in the SMA wire than in the case of a 6% stretch).

## 5. Results

Section 5.1 presents first observations in the strain response of beam #3. Section 5.2 compares tests #3, #4 and #5 in terms of total residual forces in the SMA wires at the end of the procedure (*i.e.* after cooling down to ambient temperature). Finally, Section 5.3 provides additional information about tests #1 and #2 featuring a “too high” pre-stretch level of the SMA wires ( $\varepsilon_{\max} = 6\%$ , compared to 3% for tests #3, #4 and #5).

### 5.1 Overall observations from test #3

The change in the strain in the course of time at the top and bottom surfaces of beam #3 is shown in Fig. 8; negative values correspond to contraction whereas positive values correspond to expansion. Accordingly, the top and bottom surfaces of the concrete beam are subjected to compression and tension respectively during the experiment. As expected, the strain magnitude is higher at the bottom face than at the top one, due to the tensile force created in the SMA wires by thermal activation of the memory effect. Indeed, the wires being located above the top side of the beam, the neutral axis is moved up from the symmetry axis of the beam cross-section towards its top face. Strains first increased (see Arrow 1) then stabilized (Arrow 2) during heating: maximum strain values reached at the top and the bottom faces are denoted  $\varepsilon_{t,\max}$  and  $\varepsilon_{b,\max}$  respectively. Note that the initial fluctuation (Arrow 1) is due to the manual monitoring of the heating by Joule effect. Cooling down to ambient temperature was accompanied by a sharp strain decrease (Arrow 3). This means that a significant reverse  $A \rightarrow M$  transformation occurred. However, non-null strains are obtained at the end of procedure (Arrow 4), meaning that a prestress state remained in the beam at ambient procedure: values of the residual strains are denoted  $\varepsilon_{t,\text{res}}$  and  $\varepsilon_{b,\text{res}}$  at the top and bottom surfaces respectively.

## 5.2 Comparison between tests #3, #4 and #5

Figure 9 shows the comparison between tests #3, #4 and #5, featuring a total SMA cross-section of 3.9 mm<sup>2</sup>, 15.7 mm<sup>2</sup> and 21.2 mm<sup>2</sup> respectively. Very similar trends are observed for each test. Note that the sudden strain increases that occurred during the heating steps for tests #4 and #5 (see Arrows 5 and 6) are due to the manual increase in current intensity. The cooling stages were accompanied by an almost instantaneous strain decrease, except for test #4 where strains first increased slightly (Arrows 7) before decreasing. Maximum and residual values of the strain recorded on the both sides of the beams at the end of heating and cooling steps respectively are reported in Table 4.

Considering the linearity of the concrete mechanical behavior at low stresses, it is possible to derive the total tensile force  $F_{SMA}$  developed in the SMA wires during the test from the concrete strains measured on the upper and lower surfaces of the beam, as follows:

$$F_{SMA} = E_c A_c \frac{\varepsilon_t + \varepsilon_b}{2} \quad (1)$$

where:

- $E_c$  is the Young's modulus of the concrete, taken equal to 36.2 GPa (see Section 3);
- $A_c$  is the area of the concrete beam cross-section, *i.e.*  $A_c = 40 \times 100 = 4000 \text{ mm}^2$ ;
- $\varepsilon_t$  and  $\varepsilon_b$  are the strain values given by the top and bottom gauges respectively.

From the values of  $\varepsilon_t$  and  $\varepsilon_b$  in Table 4, maximum stresses at the top and bottom faces of the concrete beam can be estimated to a few MPa, which is much lower than the compressive and tensile strengths of the material reported in Section 3.

It is then possible to calculate the corresponding stress in the SMA wires:

$$\sigma_{SMA} = \frac{F_{SMA}}{A_{SMA}} \quad (2)$$

where  $A_{SMA}$  values are given in Table 3.

The values  $F_{\text{SMA,max}}$  and  $F_{\text{SMA,res}}$  of the total force in the SMA wires and the corresponding stress values  $\sigma_{\text{SMA,max}}$  and  $\sigma_{\text{SMA,res}}$ , calculated at the end of the heating and cooling steps respectively, are reported in Table 4 for the three tests #3, #4 and #5. Figure 10 shows the values of the final force  $F_{\text{SMA,res}}$  at the end of the experimental procedure (*i.e.* after cooling down to ambient temperature) as a function of the total SMA cross-sectional area  $A_{\text{SMA}}$ . Simulation results are also displayed (see Section 6). The fairly linear trend is *a priori* fortuitous, given the different transformation temperatures of the three types of NiTi SMA wires (see Table 1) and the different thermal conditions (see  $T_{\text{max}}$  in Table 3). However, the fact that the condition  $M_s < T_{\text{amb}} \approx 0^\circ\text{C} < A_s$  with close values of  $A_s$  probably participates in obtaining such a simple trend as a function of the total SMA cross-section area.

### 5.3 Additional remarks about tests #1 and #2

Finally, Figure 11 shows the time evolution of the total force in the SMA wires for the tests #1 and #2 performed with a “too high” pre-stretch for the SMA wires ( $\varepsilon_{\text{max}} = 6\%$ ). Test conditions were nearly the same, expected concerning the maximum temperatures ( $T_{\text{max}} = 60^\circ\text{C}$  and  $45^\circ\text{C}$  respectively, see Table 3). Two comments can be done from this graph:

- as expected for the heating stage, the higher the temperature, the higher the force level reached in the SMA wires, which increases the risk of concrete failure;
- the residual force at the end of the procedure for test #2 ( $F_{\text{SMA,res}} = 1.7$  kN) appears to be lower than that for test #5 ( $F_{\text{SMA,res}} = 2.4$  kN, see Table 4) although the pre-stretch level was higher in the former case (all other parameters being otherwise practically equal, see Table 3). This could be explained by micro-cracks appearing in the concrete beam upon heating phase: see Section 6.3 about stress levels in the concrete beam as a function of the pre-stretch level and maximum temperature.

To prevent premature damage in the concrete beams during the heating step, a compromise should be found between pre-stretch level and maximum temperature to be applied before cooling down to ambient temperature. This point is discussed in the next section from a numerical model.

## 6. Modelling

### 6.1. Bases of the model

A macroscopic model was developed to analyze the stress creation during the heating-cooling cycle of the SMA wires. The simulations are based on a SMA behavior in uniaxial tension considering three internal variables: wire temperature  $T$ , strain  $\varepsilon_{\text{SMA}}$  and martensite volume fraction  $z$ . Phase changes in NiTi-based SMA wires are generally associated with the propagation of transformation fronts separating austenite and martensite [38-41], which leads to complex thermomechanical couplings in the case of heterogeneous temperature distribution. For the sake of simplicity, the three variables  $T$ ,  $\varepsilon_{\text{SMA}}$  and  $z$  were here considered as homogeneous within the wires. The mechanical coupling between the SMA wires and the concrete beam was written through the following equality that must be fulfilled at any temperature  $T$ :

$$L_{\text{SMA}_1}(T) = L_{\text{SMA}_2}(T) \quad (3)$$

where  $L_{\text{SMA}_1}$  and  $L_{\text{SMA}_2}$  are the length of the SMA wires calculated from the deformation of the concrete beam and the wires respectively. In the bent beam, the former length can be calculated as follows:

$$L_{\text{SMA}_1}(T) = (1 + \varepsilon_{\text{c\_normal}}(T) - \chi_{\text{c}}(T) \times h_{\text{SMA}}) \times L_0 \quad (4)$$

where:

- $L_0$  is the initial length of the unstressed beam, same as the length of the pre-stretched wires installed on the concrete beam at zero stress (see Fig. 5-a):  $L_0 = 500$  mm;
- $h_{\text{SMA}}$  is the distance of the SMA wires' centroid to the centroid of the concrete beam (see Fig. 6):  $h_{\text{SMA}} = 70$  mm;
- $\varepsilon_{\text{c\_normal}}$  and  $\chi_{\text{c}}$  are the longitudinal strain (due to the normal force) and the curvature (due to bending) of the concrete beam. The static equilibrium enables us to express these two quantities as a function of the actual stress  $\sigma_{\text{SMA}}(T)$  in the SMA wires:

$$\varepsilon_{c\_normal}(T) = \frac{-A_{SMA} \times \sigma_{SMA}(T)}{E_c \times A_c} \quad (5)$$

$$\chi_c(T) = \frac{h_{SMA} \times A_{SMA} \times \sigma_{SMA}(T)}{E_c \times I_c} \quad (6)$$

Let us recall the parameters already introduced in the previous sections: concrete Young's modulus:  $E_c = 36.2$  GPa; cross-section area of the concrete beam:  $A_c = 4000$  mm<sup>2</sup>; total cross-section area of SMA wires  $A_{SMA}$ . Finally,  $I_c$  is the quadratic momentum of the concrete beam cross-section (height  $h = 100$  mm and width  $b = 40$  mm):  $I_c = 3.33 \times 10^6$  mm<sup>4</sup>.

The current length of the SMA wires can be also calculated from their strain  $\varepsilon_{SMA}$ :

$$L_{SMA\_2}(T) = (1 + \varepsilon_{SMA}(T)) \times L_0 \quad (7)$$

The SMA strain can be split in an elastic part, a thermal part and a phase transformation part as follows:

$$\varepsilon_{SMA}(T) = \frac{\sigma_{SMA}(T)}{E_{SMA}(z)} + \alpha_{SMA} \times (T - T_{amb}) + z \times \gamma \quad (8)$$

Let us recall that the martensite volume fraction  $z$  depends on stress and temperature, *i.e.*  $z(\sigma_{SMA}(T), T)$ . In Eq. (8),  $\gamma$  is the total phase transformation strain of the SMA wires, taken equal to 6% for the three types of SMA wires. Symbols  $E_{SMA}$  and  $\alpha_{SMA}$  correspond to the apparent Young's modulus and coefficient of thermal expansion (CTE) respectively. A mixing law was used to define these two quantities as a function of the martensite volume fraction:

$$E_{SMA}(z) = \phi \times [(1 - z) \times E_{aust} + z \times E_{mart}] \quad (9)$$

$$\alpha_{SMA}(z) = (1 - z) \times \alpha_{aust} + z \times \alpha_{mart} \quad (10)$$

Because of the difficulties in identifying the Young' modulus of NiTi SMAs, we preferred to consider the typical values for NiTi SMAs in the literature [36]:  $E_{aust} = 65$  GPa and  $E_{mart} = 25$  GPa. However, a corrective coefficient  $\phi$  was applied for the additional

compliance due to the connection at the ends of the wires (see Section 2.2). CTE values for austenite ( $\alpha_{\text{aust}}$ ) and martensite ( $\alpha_{\text{mart}}$ ) were identified in Section 2.1: see Table 1.

Different laws have been proposed in the literature to obtain the evolution of the martensite volume fraction  $z$  along a path in the stress-temperature space. In the present work, we simply considered *linear* variations for  $z$  in the two transformation domains A→M and M→A with the following condition:  $z$  is not allowed to increase (decrease, respectively) in the M→A transformation domain (A→M transformation domain, respectively). The two domains are built from the four transformation temperatures at zero stress identified in Section 2.1 (see Table 1) and the slope  $\beta$  defining the linear effect of the stress on the transformation temperatures: see Fig. 12-a.  $\beta$  can be defined by the ratio  $\sigma_{\text{cr}}/(T_{\text{amb}} - M_s)$  from the data in Tables 1 and 2. Table 5 sums up the additional parameter values used for the simulations. Note that typical values for  $\beta$  in the literature are about 6–8 MPa per °C [35]. The lower value for the 1 mm diameter wire ( $\beta = 4.9$ ) could be explained by the fact that the  $M_s$  value is closer to the ambient temperature in the case of the 1 mm diameter wire ( $M_s = -7^\circ\text{C}$ , see Table 1) than in the two other cases ( $M_s = -11^\circ\text{C}$  and  $-30^\circ\text{C}$  for the 2 mm and 3 mm diameter wires respectively), leading to a greater uncertainty in the calculation of the  $\sigma_{\text{cr}}/(T_{\text{amb}} - M_s)$  ratio. Although the used SMA model is simple, it provides a tool to discuss the qualitative trends of the experimental results.

In practice for any temperature value  $T$ , an iterative procedure was implemented to find the stress value  $\sigma_{\text{SMA}}(T)$  enabling Eq. 3 to be fulfilled. Over the iterations, the stress value is increased or decreased depending on the error defined as follows:

$$Error = \frac{L_{\text{SMA}_1}(T) - L_{\text{SMA}_2}(T)}{L_0} \quad (11)$$

A criterion is used for convergence: the latter is considered as reached when  $|Error|$  is lower than  $10^{-8}$ . Finally, in post-process, the longitudinal strains  $\varepsilon_t$  and  $\varepsilon_b$  on the top and bottom faces of the concrete beam can be calculated:

$$\varepsilon_t(T) = \varepsilon_{\text{c\_normal}}(T) + \chi_c(T) \times \frac{h}{2} \quad (12)$$

$$\varepsilon_b(T) = \varepsilon_{c\_normal}(T) - \chi_c(T) \times \frac{h}{2} \quad (13)$$

## 6.2. Analysis and comparison with the experiments

Figure 12 presents the simulation results corresponding to the experimental conditions of test #3. Figure 12-a first shows the path in the stress-temperature plane for the SMA wires. Upon heating, the stress  $\sigma_{SMA}$  remains equal to zero until the Austenite-start temperature  $A_s$  is reached (step 1). The martensite volume fraction  $z$  remains constant and equal to 0.40 in the present case: see Fig. 12-b. Next, the  $M \rightarrow A$  transformation occurs (step 2), leading to a decrease in the martensite volume fraction. The memory effect being thus activated, the decrease in length of the SMA wires is accompanied by a stress increase due to coupling with the concrete beam. This explains why the  $M \rightarrow A$  transformation is not completed at the maximum temperature  $T_{max}$  although the latter is higher than the Austenite-finish temperature  $A_f$ : see the corresponding point in Fig. 12-a, which is still inside the  $M \rightarrow A$  transformation domain. The martensite volume fraction decreases to the value of 0.27 at the maximum temperature (Fig. 12-b). Upon cooling, the martensite volume fraction first remains equal to 0.27 (step 3), then increases when entering the  $A \rightarrow M$  transformation domain (step 4). Note that the slight increase in stress during step 3 is due to the thermal contraction. The creation of martensite in step 4 is accompanied by a strong stress decrease due to the increase in the length of the SMA wires. Figure 12-c shows the variation of the strain at the top and bottom surfaces of the concrete beam as a function of the SMA temperature. Similar simulation results are obtained with the experimental conditions of tests #4 and #5. They are in agreement with the experimental results, except that the slight strain increase in Step 3 (Fig. 12-c) was observed only in the experimental test #4 (see Arrows 7 in Fig. 9). This can be explained by the simplicity of the SMA model used in the simulations. However, the dissymmetry in strain between the top and bottom surfaces of the concrete beam is correctly captured by the model. Finally, the comparison between experimental and numerical results can be done from Figure 10 above, showing the total force  $F_{SMA,res}$  in the SMA wires at end of the experimental procedure (*i.e.* after cooling down to ambient temperature) as function of the total cross-section area  $A_{SMA}$  of SMA wires. A good agreement is observed between experimental and numerical values, enabling us to go further in the use of the model to analyze the compromise to be respected between pre-stretch level and maximum temperature to avoid concrete beam failure.

### 6.3. Discussion about the compromise between maximum SMA temperature and pre-strain

The following ranges of pre-strain  $\varepsilon_{\max}$  and maximum temperature  $T_{\max}$  were numerically browsed: [0.3%; 8%] and [ $T_{\text{amb}}$ ; 100°C]. The same ambient temperature was considered for all the simulations:  $T_{\text{amb}} = 1^\circ\text{C}$ , which is the mean value of experimental tests #1 to #5 (see Table 3). Let us note that for any value of  $\varepsilon_{\max}$ , the initial value for the martensite volume fraction at the beginning of the heating-cooling cycle must be preliminary calculated as a function of the pre-strain  $\varepsilon_{\max}$ . This quantity  $z(0 \text{ MPa}, T_{\text{amb}})$  is referred to as  $z_{\text{init}}$  in the rest of the text for ease of writing. It is defined as the ratio of the residual strain (after stretching at  $\varepsilon_{\max}$  and unloading) to the total phase transformation strain of the SMA wires  $\gamma$ :

$$z_{\text{init}} = \frac{\varepsilon_{\max} - \frac{\sigma_{\max}}{E_{\text{SMA}}(z_{\text{init}})}}{\gamma} \quad (14)$$

where it can be noted that the quantity  $\sigma_{\max}/E_{\text{SMA}}(z_{\text{init}})$  corresponds to the elastic strain recovered upon unloading. The stress  $\sigma_{\max}$  at strain  $\varepsilon_{\max}$  can be simply defined as the sum of the Martensite-start stress  $\sigma_{\text{cr}} = \beta \times (T_{\text{amb}} - M_s)$  and the proportion  $z_{\text{init}}$  of the stress amplitude  $\beta \times (M_f - M_s)$  corresponding to a full transformation from austenite to martensite. Thus:

$$\sigma_{\max} = \beta \times (T_{\text{amb}} - M_s) + z_{\text{init}} \times \beta \times (M_f - M_s) \quad (15)$$

It can be noted that finding  $z_{\text{init}}$  from Eqs (14) and (15) is not trivial as the right-hand side of the former equation depends on the value to be identified. Moreover,  $z_{\text{init}}$  is constrained between 0 (pure austenite) and 1 (pure martensite). The identification of  $z_{\text{init}}$  for any strain value  $\varepsilon_{\max}$  was therefore performed numerically by iterative approach.

Figure 13 shows the maps of total force  $F_{\text{SMA, res}}$  in the SMA wires at end of the heating-cooling cycle as a function of the pre-strain  $\varepsilon_{\max}$  and maximum temperature  $T_{\max}$ .

Moreover, configurations for which concrete failure is expected at the bottom surface of the beam are indicated in the graphs:

$$\text{Concrete beam failure: } \max \{E_c \times \varepsilon_b(T)\} > 4 \text{ MPa} \quad (16)$$

where the value of 4 MPa was defined from the tensile strengths indicated in Section 3 (4.4 MPa for the cylinders and 4.1 MPa for the cubes). The following comments can be done from Fig. 13:

- no concrete beam failure was obtained for the case of five 1 mm diameter wires, whereas failure is possible in the cases of five 2 mm diameter wires and three 3 mm diameter wires: compare Fig. 13-a with Figs 13-b and -c;
- the points corresponding to the experimental tests #1 to #5 are also placed in the graphs. It is interesting to note that the point corresponding to test #1 is correctly located in the failure domain of the concrete beam: see Fig. 13-c. The point corresponding to test #2 is located very close to the boundary of the failure domain, which may explain the low value of residual force  $F_{\text{SMA, res}}$  that was observed experimentally, without beam failure (see Section 5.3);
- globally, the higher the pre-strain  $\varepsilon_{\text{max}}$ , the higher the total residual force  $F_{\text{SMA, res}}$  in the SMA wires. Same for the influence of the maximum temperature  $T_{\text{max}}$ . Maximum values for  $F_{\text{SMA, res}}$  are indicated in the color bars for each case: 0.57 kN, 2.3 kN and 4.3 kN for the five 1 mm, five 2 mm and three 3 mm diameter wires respectively. However, these maximum values are obtained at the boundary of the failure domains, making them tricky to obtain experimentally.

## 7. Conclusion

The memory effect of SMAs has opened perspectives to create prestress states in concrete elements. However, the procedure has not yet been fully resolved because of practical difficulties of mechanical coupling between SMA and concrete elements, and also because of the complex thermomechanical behavior of these alloys. The present study focused on the development of the prestressing forces during the thermal cycle required in the procedure for the activation of the memory effect in the SMA. Strain measurements were

performed on concrete prismatic with external NiTi SMA wires, and a numerical model was developed to simulate the strain evolution in the concrete beams during the heating-cooling cycle of the SMA wires. Following conclusions can be drawn from the study:

- as the concrete failure may occur during the heating step, a compromise should be found between the SMA pre-stretch level and the maximum temperature to be applied before returning to ambient temperature;
- the higher the pre-stretch level of the SMA wires, the higher the prestresses. Same for the influence of the maximum temperature reached during the heating step. However, the maximum prestressing forces are obtained at the boundary of the failure domain of the concrete beam, making them tricky to obtain experimentally.

Results obtained should not make forget the complexity of the mechanical coupling between the SMA wires and the concrete beam. Anchorages embedded in the concrete would probably lead to higher prestressing forces, but also higher maximal stresses during the heating step. The complex thermomechanical response of SMAs requires a particular attention in the definition of the ambient temperature and heating conditions to avoid concrete failure.

## **Compliance with ethical standards**

### *Conflict of interest*

The authors declare that they have no conflict of interest.

### *Ethical issues*

The authors declare the compliance with the ethical standards.

## **References**

- [1] Otsuka K, Wayman CM. Shape memory materials. Cambridge, UK: Cambridge University Press; 1999.

- [2] Lexcelent C. Shape-memory alloys handbook. London, UK & Hoboken, NJ, USA: ISTE & Wiley; 2013.
- [3] Ziółkowski A. Pseudoelasticity of Shape Memory Alloys: Theory and Experimental Studies. Oxford, UK: Butterworth-Heinemann; 2015.
- [4] Lagoudas DC. Shape Memory Alloys: Modeling and Engineering Applications. New York: Springer US; 2010.
- [5] Zbiciak A, Wasilewski K. Constitutive modelling and numerical implementation of SMA material with internal loops. *Arch Civ Eng*. 2018;64:211-32.
- [6] Debska A, Balandraud X, Destrebecq JF, Gwozdziwicz P, Seruga A. Influence of thermal boundary effects on the process of creating recovery stresses in a SMA wire activated by Joule heating. *J Mater Eng Perform*. 2017;26:3336–46.
- [7] Mazzolani FM, Mandara A. Modern trends in the use of special metals for the improvement of historical and monumental structures. *Eng Struct*. 2002;24:843–56.
- [8] Song G, Ma N, Li HN. Review of applications of shape memory alloys in civil structures. In: Malla RB, Maji A, editors. *Engineering, Construction and Operations in Challenging Environments: earth and space*. New York, NY, USA: Amer Soc Civil Engineers; 2004. pp. 559–66.
- [9] Song G, Ma N, Li HN. Application of shape memory alloys in civil structures. *Eng Struct*. 2006;28:1266–74.
- [10] Janke L, Czaderski C, Motavalli M, Ruth J. Applications of shape memory alloys in civil engineering structures – Overview, limits and new ideas. *Mater Struct*. 2005;38:578–92.
- [11] Alam MS, Youssef MA, Nehdi M. Utilizing shape memory alloys to enhance the performance and safety of civil infrastructure: a review. *Can J Civil Eng*. 2007;34:1075–86.
- [12] Motavalli M, Czaderski C, Bergamini A, Janke L. Shape memory alloys for civil engineering structures – on the way from vision to reality. 6th International Conference (AMCM'2008). June 6-11, 2008; Łódź, Poland; 2008. pp. 91–108.
- [13] Motavalli M, Czaderski C, Bergamini A, Janke L. Application of shape memory alloys in civil engineering; past, present and future. 17th International Conference on Composites or Nano Engineering (ICCE 17). 26 July - 1 August 2009. Honolulu (T.H.), USA.
- [14] Cladera A, Weber B, Leinenbach C, Czaderski C, Shahverdi M, Motavalli M. Iron-based shape memory alloys for civil engineering structures: An overview. *Constr Build Mater*. 2014;63:281–93.

- [15] Dong JH, Cai CS, Okeil AM. Overview of potential and existing applications of shape memory alloys in bridges. *J Bridge Eng.* 2011;16:305–15.
- [16] Casciati S. SMA-based devices: insight across recent proposals toward civil engineering applications. *Smart Struct Syst.* 2019;24:111–25.
- [17] Zhao H, Andrawes B. Innovative prestressing technique using curved shape memory alloy reinforcement. *Constr Build Mater.* 2020;238:117687.
- [18] Shahverdi M, Czaderski C, Annen P, Motavalli M. Strengthening of RC beams by iron-based shape memory alloy bars embedded in a shotcrete layer. *Eng Struct.* 2016;117:263–73.
- [19] Rojob H, El-Hacha R. Performance of RC beams strengthened with self-prestressed Fe-SMA bars exposed to freeze-thaw cycles and sustained load. *Eng Struct.* 2018;169:107–18.
- [20] Miralami M, Esfahani MR, Tavakkolizadeh M. Strengthening of circular RC column-foundation connections with GFRP/SMA bars and CFRP wraps. *Compos Part B-Eng.* 2019;172:161–72.
- [21] Oudah F, El-Hacha R. Joint performance in concrete beam-column connections reinforced using SMA smart material. *Eng Struct.* 2017;151:745–60.
- [22] Fritsch E, Izadi M, Ghafoori E. Development of nail-anchor strengthening system with iron-based shape memory alloy (Fe-SMA) strips. *Constr Build Mater.* 2019;229:117042.
- [23] Alam MS, Youssef MA, Nehdi M. Utilizing shape memory alloys to enhance the performance and safety of civil infrastructure: a review. *Can J Civil Eng.* 2007;34:1075–86.
- [24] Andrawes B, Shin M, Wierschem N. Active Confinement of Reinforced Concrete Bridge Columns Using Shape Memory Alloys. *J Bridge Eng.* 2010;15:81–9.
- [25] El-Hacha R, Abdelrahman K. Behaviour of circular SMA-confined reinforced concrete columns subjected to eccentric loading. *Eng Struct.* 2020;215:110443.
- [26] Abdelrahman K, El-Hacha R. Analytical prediction model for circular SMA-confined reinforced concrete columns. *Eng Struct.* 2020;213:110547.
- [27] Karhu M, Lindroos T. Long-term behaviour of binary Ti–49.7Ni (at.%) SMA actuators—the fatigue lives and evolution of strains on thermal cycling. *Smart Mater Struct.* 2010;19:11.
- [28] ASTM F2004-05(2010). Standard Test Method for Transformation Temperature of Nickel-Titanium Alloys by Thermal Analysis. ASTM International, West Conshohocken, PA, 2010. <https://doi.org/10.1520/F2004-05R10>

- [29] Gądek S, Hebda M, Kazior J. Zastosowanie dylatometrii w badaniach przemysłowych na przykładzie proszku ferrytycznej stali nierdzewnej AISI 434L. *Czasopismo Techniczne. Mechanika / Technical Transactions. Mechanics*. Vol. R. 109, z. 9-M. Kraków: Wydawnictwo PK; 2012. pp. 77–87.
- [30] Destrebecq JF, Balandraud X. Interaction between concrete cylinders and shape-memory wires in the achievement of active confinement. In: Ochsner A et al., editors. *Materials with Complex Behaviour: Modelling, Simulation, Testing, and Applications. Advanced Structured Materials*. Berlin: Springer-Verlag Berlin; 2010. Vol. 3, pp. 19–34. [https://doi.org/10.1007/978-3-642-12667-3\\_2](https://doi.org/10.1007/978-3-642-12667-3_2)
- [31] Tran H, Balandraud X, Destrebecq JF. Recovery stresses in SMA wires for civil engineering applications: experimental analysis and thermomechanical modelling. *Materialwiss Werkst.* 2011;42:435–43.
- [32] Debska A, Balandraud X, Gwozdziwicz P, Destrebecq JF, Seruga A. An experimental study of the use of shape memory alloy for the prestressing of small scale concrete beams. *AMCM 2011: 7th International Conference Analytical Models and New Concepts in Concrete and Masonry Structures*. June 13–15, 2011, Crakow, Poland.
- [33] Tran H, Balandraud X, Destrebecq JF. Improvement of the mechanical performances of concrete cylinders confined actively or passively by means of SMA wires. *Arch Civ Mech Eng.* 2015;15: 292–99.
- [34] Debska A, Balandraud X, Destrebecq JF, Seruga A, Gwozdziwicz P. Badania betonowych belek sprężonych zewnętrznie wstępnie odkształconym drutem z pamięcią kształtu (SMA). In: Derkowski W et al., editors. *Konferencja Naukowo-Techniczna Konstrukcje Sprezone (KS2018)*, April 18–20, 2018, Cracow, Poland. Politechnika Krakowska; 2018. pp. 83–86.
- [35] Heller L, Seiner H, Šittner P, Sedlák P, Tyca O, Kadeřávek L. On the plastic deformation accompanying cyclic martensitic transformation in thermomechanically loaded NiTi. *Int J Plasticity.* 2018;111:53–71.
- [36] Sittner P, Heller L, Pilch J, Curfs C, Alonso T, Favier D. Young's modulus of austenite and martensite phases in superelastic NiTi wires. *J Mater Eng Performance* 2014;23:2303–14.
- [37] Instrukcja Instytutu Techniki Budowlanej. *Laboratoria Budowlane. Praca zbiorowa* (in Polish; *Instruction of Institut Techniki Budowlanej. Construction Laboratories*) Instytut Techniki Budowlanej Warszawa 1971, s.1-196. Poland.

- [38] Favier D, Louche H, Schlosser P, Orgeas L, Vacher P, Debove L. Homogeneous and heterogeneous deformation mechanisms in an austenitic polycrystalline Ti-50.8 at.% Ni thin tube under tension. Investigation via temperature and strain fields measurements. *Acta Mater.* 2007;55:5310–22.
- [39] Zheng L, He Y, Moumni Z. Effects of Luders-Like Bands on NiTi Fatigue Behaviors. *Int J Solids Struct.* 2016;83:28–44.
- [40] Dong L, Zhou RH, Wang XL, Hu GK, Sun QP. On interfacial energy of macroscopic domains in polycrystalline NiTi shape memory alloys. *Int J Solids Struct.* 2016;80:445–55.
- [41] Jury A, Balandraud X, Heller L, Šittner P, Karlik M. Reconstruction of heat sources induced in superelastically loaded Ni-Ti wire by localized deformation processes. *Exp Mech.* 2020;in press. DOI: 10.1007/s11340-020-00648-8

Table 1. Transformation temperatures measured by differential scanning calorimetry (DSC) and dilatometry technique. The coefficient of thermal expansion (CTE) of the austenite and martensite phases is also indicated

	Transformation temperatures [°C] measured					CTE [K <sup>-1</sup> ] measured	
	by DSC*		by dilatometry			by dilatometry	
	A <sub>s</sub>	M <sub>f</sub>	M <sub>s</sub>	A <sub>s</sub>	A <sub>f</sub>	Austenite	Martensite
Ni-Ti ø 1 mm	5	-51	-7	14	22	11E-6	7E-6
Ni-Ti ø 2 mm	9	-66	-11	2	13	10E-6	8E-6
Ni-Ti ø 3 mm	-6	-51	-30	1	10	9E-6	6E-6

\*Measurement by the supplier.

Table 2. Mechanical properties of the three Ni-Ti SMA wires at 15°C

	Diameter of the wires		
	ø 1 mm	ø 2 mm	ø 3 mm
Martensite-start stress, $\sigma_{cr}$ [MPa]	244	314	340
Stress at 6% strain, $\sigma_{max}$ [MPa]	269	309	349
Residual strain obtained, $\epsilon_{res}$ [-]	5.1	4.6	3.0
Residual stress after thermal cycle, $\sigma_{res}$ [MPa]	202	248	179

Table 3. Beam test conditions

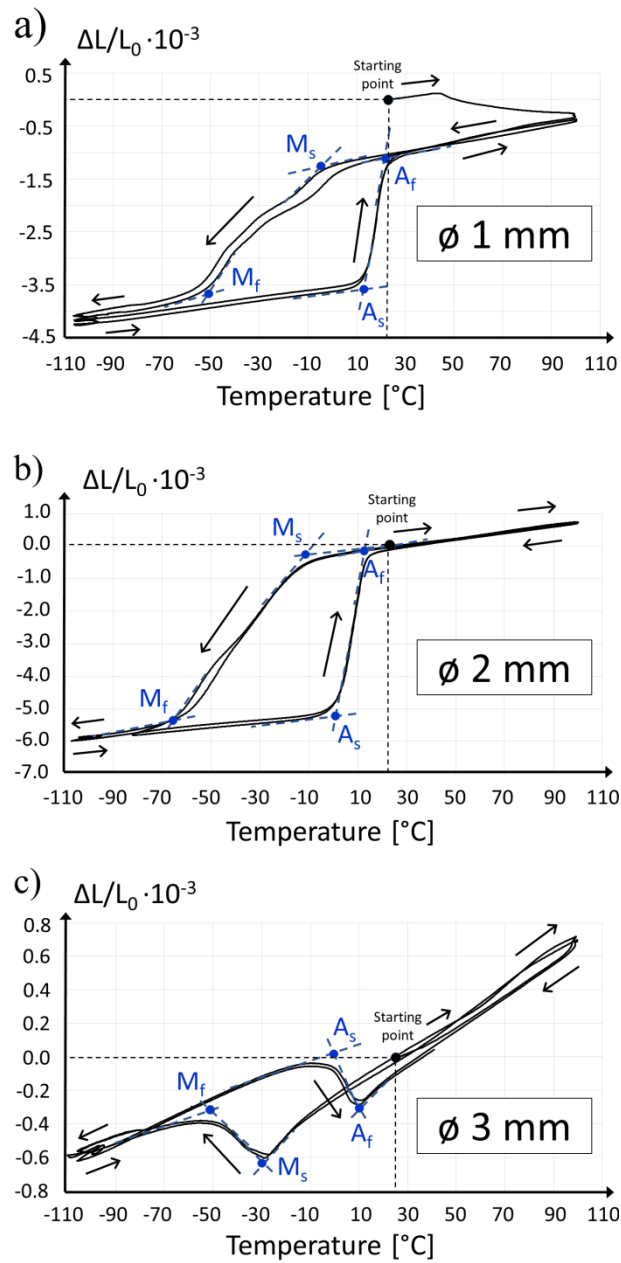
Beam #	Wire diameter	Number of wires	Wire cross-section area, $A_{SMA}$	Wire pre-stretch, $\epsilon_{max}$	Ambient temperature, $T_{amb}$	Maximum temperature, $T_{max}$	Comment
#1	3 mm	3	21.2 mm <sup>2</sup>	6%	-1°C	60°C	Failure
#2	3 mm	3	21.2 mm <sup>2</sup>	6%	1°C	45°C	
#3	1 mm	5	3.9 mm <sup>2</sup>	3%	1°C	60°C	
#4	2 mm	5	15.7 mm <sup>2</sup>	3%	0°C	20°C	
#5	3 mm	3	21.2 mm <sup>2</sup>	3%	4°C	40°C	

Table 4. Comparison between tests #3, #4 and #5

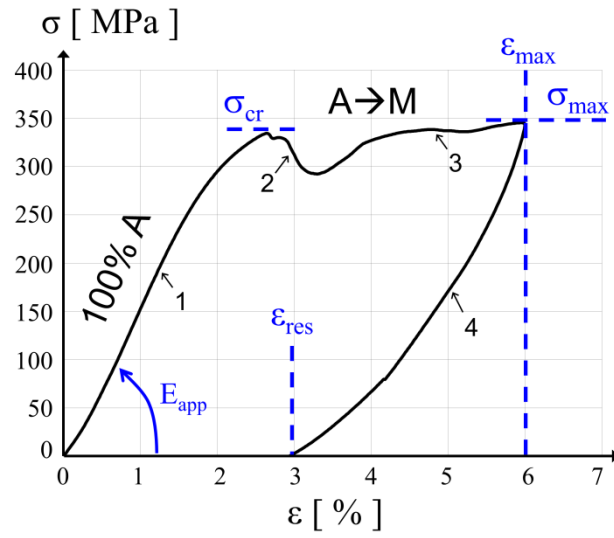
	Strains [ $10^{-6}$ ] at the concrete surface				Stress in the SMA wires		Force in the SMA wires	
	Heating		Cooling		Heating	Cooling	Heating	Cooling
	Top	Bottom	Top	Bottom				
	$\varepsilon_{t,max}$	$\varepsilon_{b,max}$	$\varepsilon_{t,res}$	$\varepsilon_{b,res}$	$\sigma_{SMA,max}$	$\sigma_{SMA,res}$	$F_{SMA,max}$	$F_{SMA,res}$
#3	-41	18	-4	5	245 MPa	43 MPa	0.96 kN	0.17 kN
#4	-132	86	-38	32	239 MPa	80 MPa	3.7 kN	1.2 kN
#5	-106	66	-83	55	139 MPa	113 MPa	2.9 kN	2.4 kN

Table 5. Additional parameters for the simulations

	Diameter of the wires		
	$\phi$ 1 mm	$\phi$ 2 mm	$\phi$ 3 mm
Young's modulus of austenite, $E_{aust}$	65 GPa	=	=
Young's modulus of martensite, $E_{mart}$	25 GPa	=	=
Corrective coefficient to account for the additional compliance due to the connection device at the wire ends (see Eq. 9), $\phi$	0.53	0.33	0.24
Slope of the transformation lines in the state diagram, $\beta$	4.9	5.8	6.3
Total phase transformation strain of the SMA wires, $\gamma$	6%	=	=



**Fig. 1** Dilatometry curves for identification of the four transformation temperatures of the three Ni-Ti SMA wires



**Fig. 2** Stress-strain diagram of the 3 mm diameter wire subjected to a load-unload cycle for a maximum strain  $\epsilon_{max}$  of 6% at an ambient temperature of 15°C

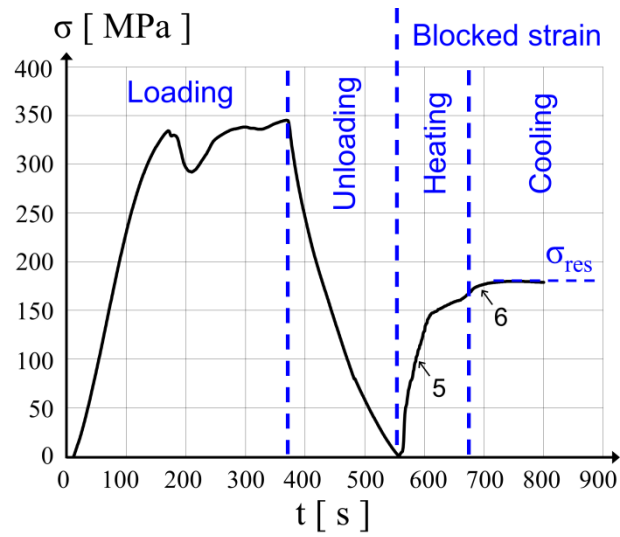


**Fig. 3** Time evolution of the stress during the test in Fig. 2 (until  $t = 560$  s), followed by the thermal cycle at blocked residual strain (from  $t = 560$  s). A residual stress  $\sigma_{res}$  of 173 MPa is obtained at the end of the experimental procedure

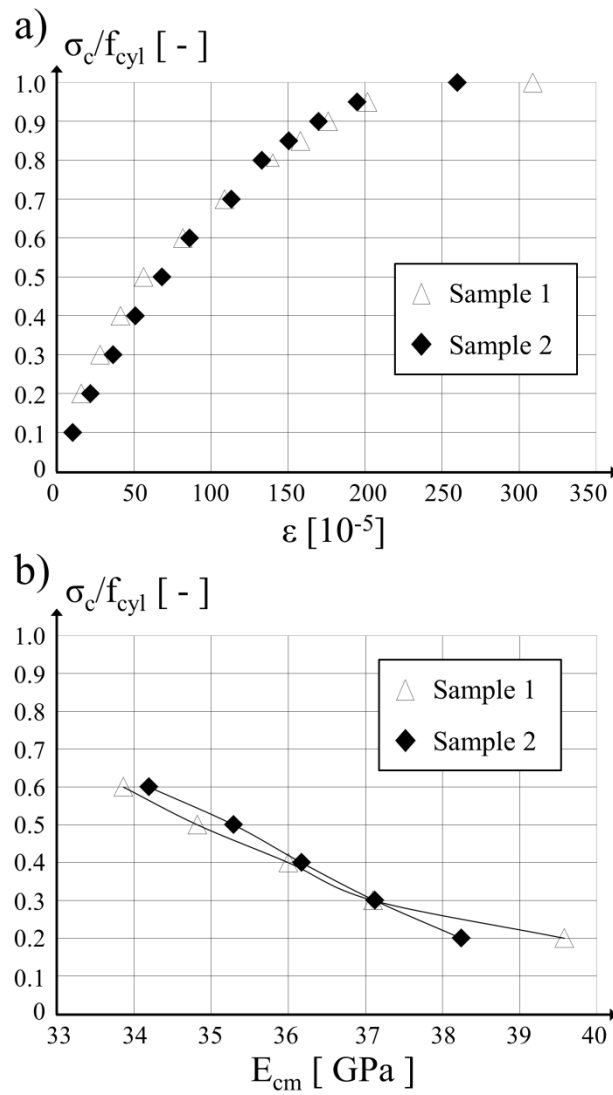


**Fig. 4** Compression tests on concrete cylinders: a) longitudinal strain vs. loading level, b) secant elastic modulus vs. loading level

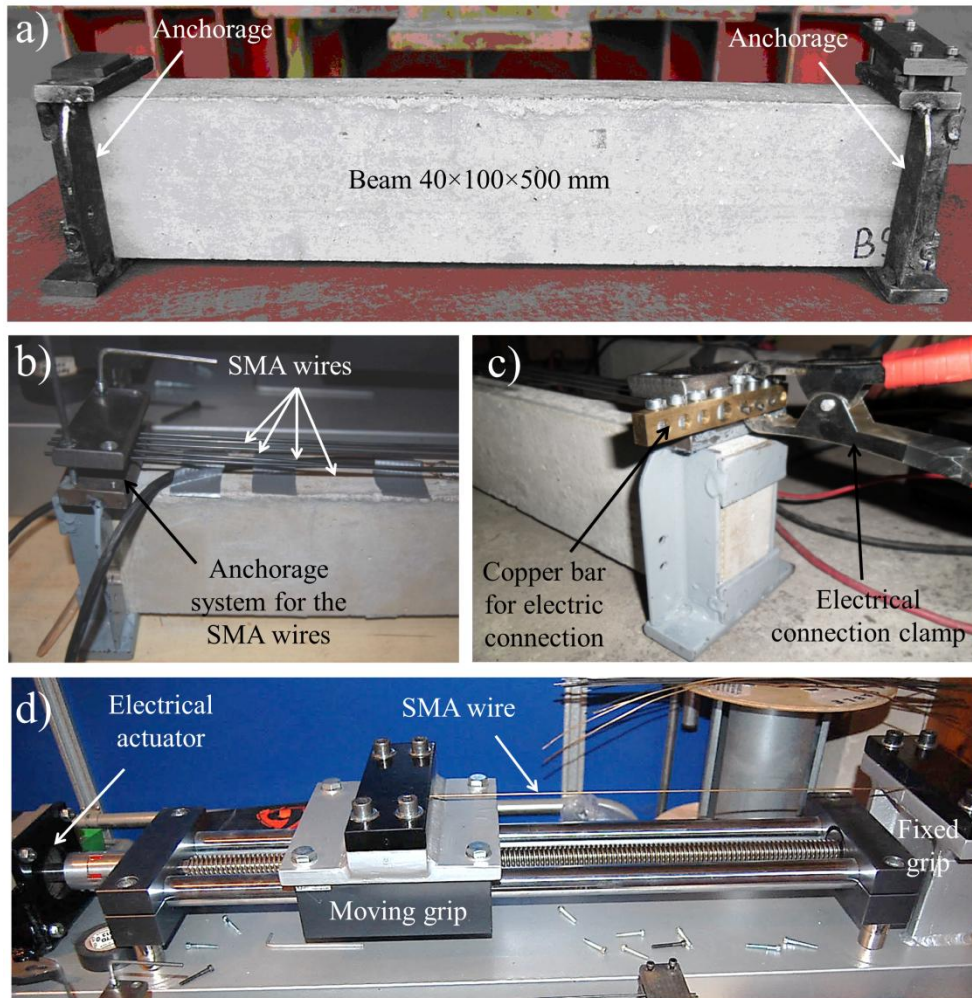


**Fig. 5** Preparation of the concrete beams equipped with SMA wires: a) beam with the two anchorages, b) fixing of the SMA wires, c) electrical connection, d) device for stretching the SMA wires before placement on the beams

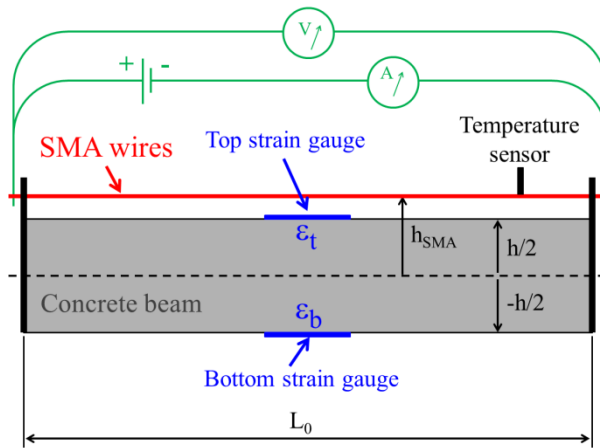


**Fig. 6** Scheme of a concrete beam equipped with SMA wires and electrical system for thermal activation by Joule effect

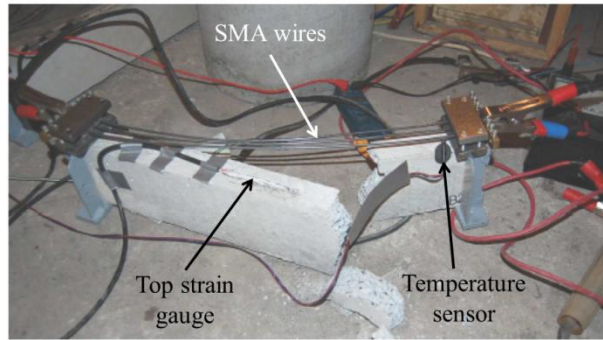


**Fig. 7** Concrete beam #1 after rupture

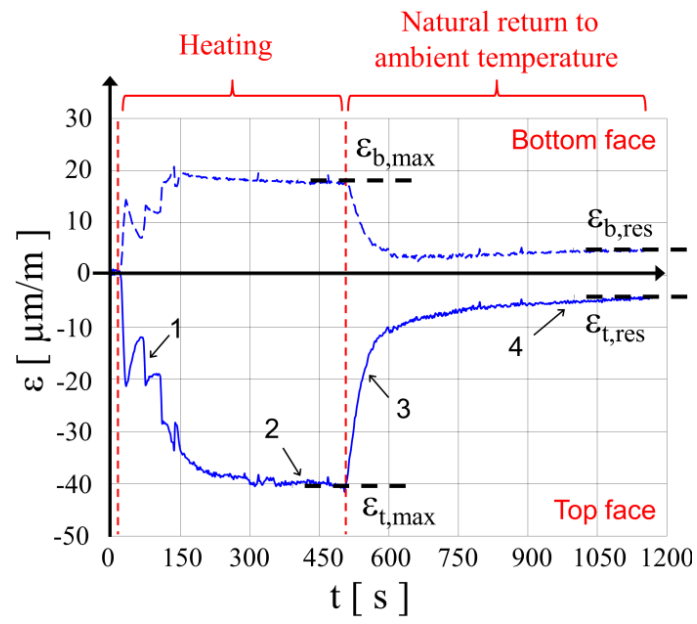


**Fig. 8** Test #3: time variation of the strain at the top and bottom surfaces of the concrete beam

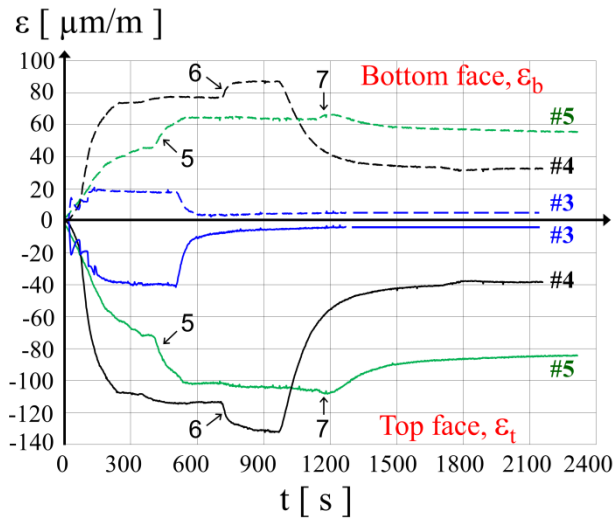


**Fig. 9** Comparison between tests #3, #4 and #5: time variation of the strain at the top and bottom surfaces of the concrete beams

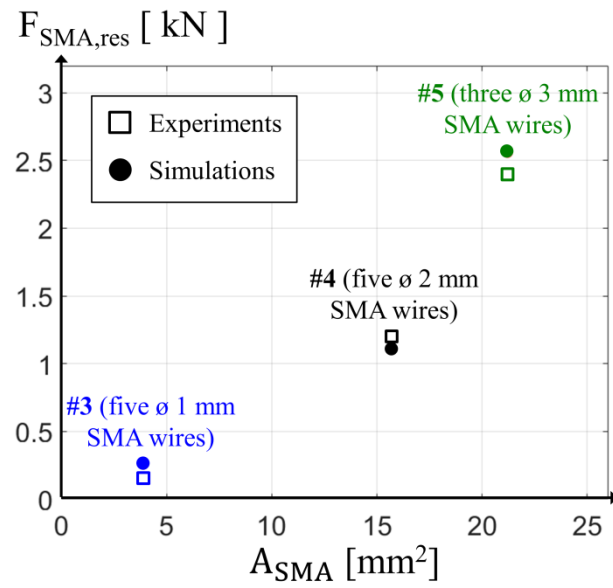


**Fig. 10** Comparison between tests #3, #4 and #5: total force  $F_{SMA,res}$  in the SMA wires at end of the experimental procedure (*i.e.* after cooling down to ambient temperature) vs. total cross-section area  $A_{SMA}$  of SMA wires

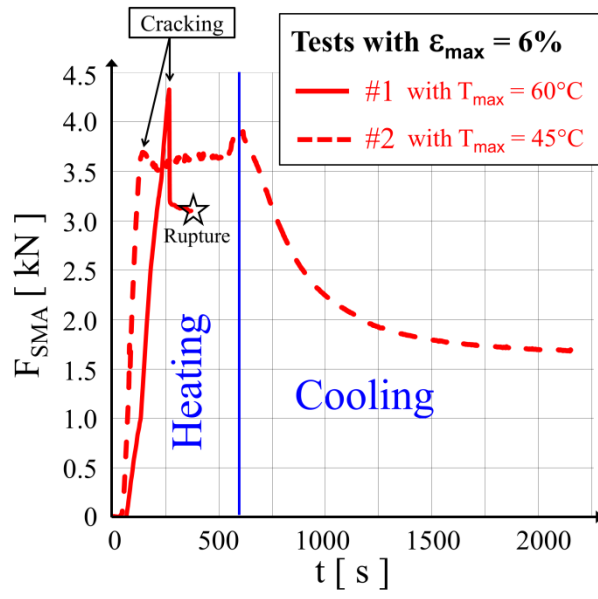


**Fig. 11** Time variation of the total force  $F_{\text{SMA}}$  in the SMA wires for the tests #1 and #2

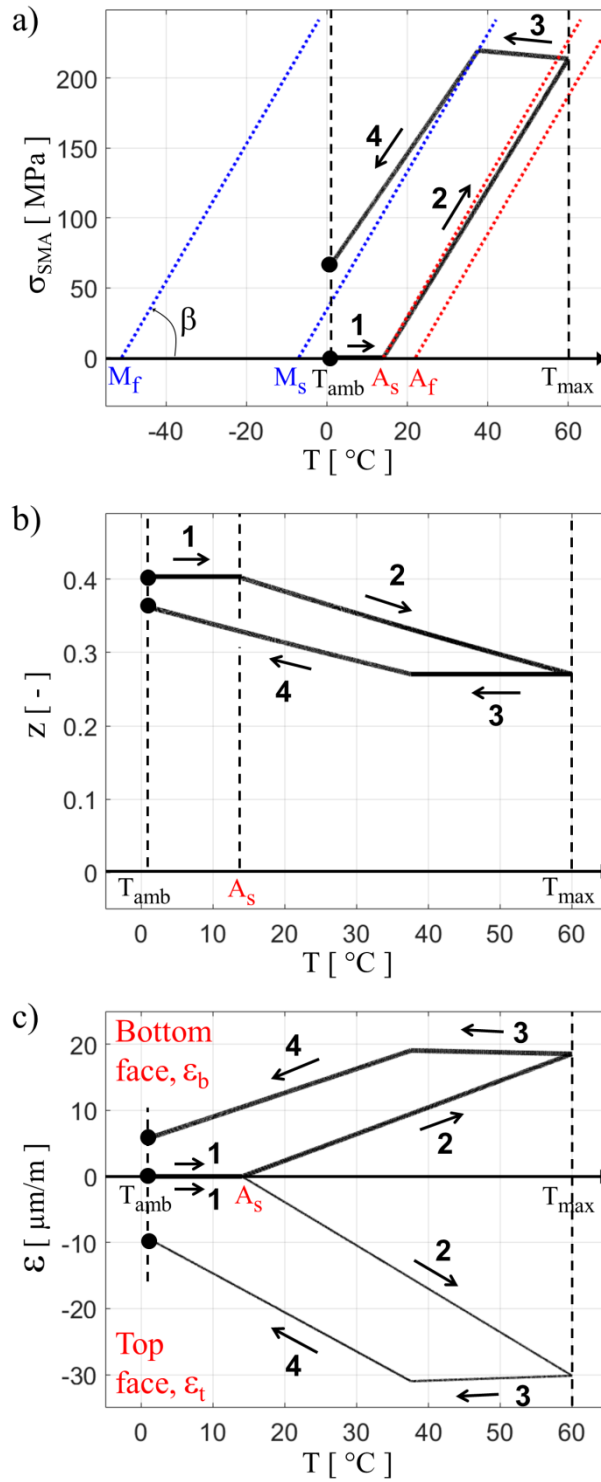


**Fig. 12** Simulation results for test #3: a) stress vs. temperature in the SMA wires, b) martensite volume fraction vs. temperature in the SMA wires, c) strain at the top and bottom surfaces of the concrete beam vs. SMA temperature

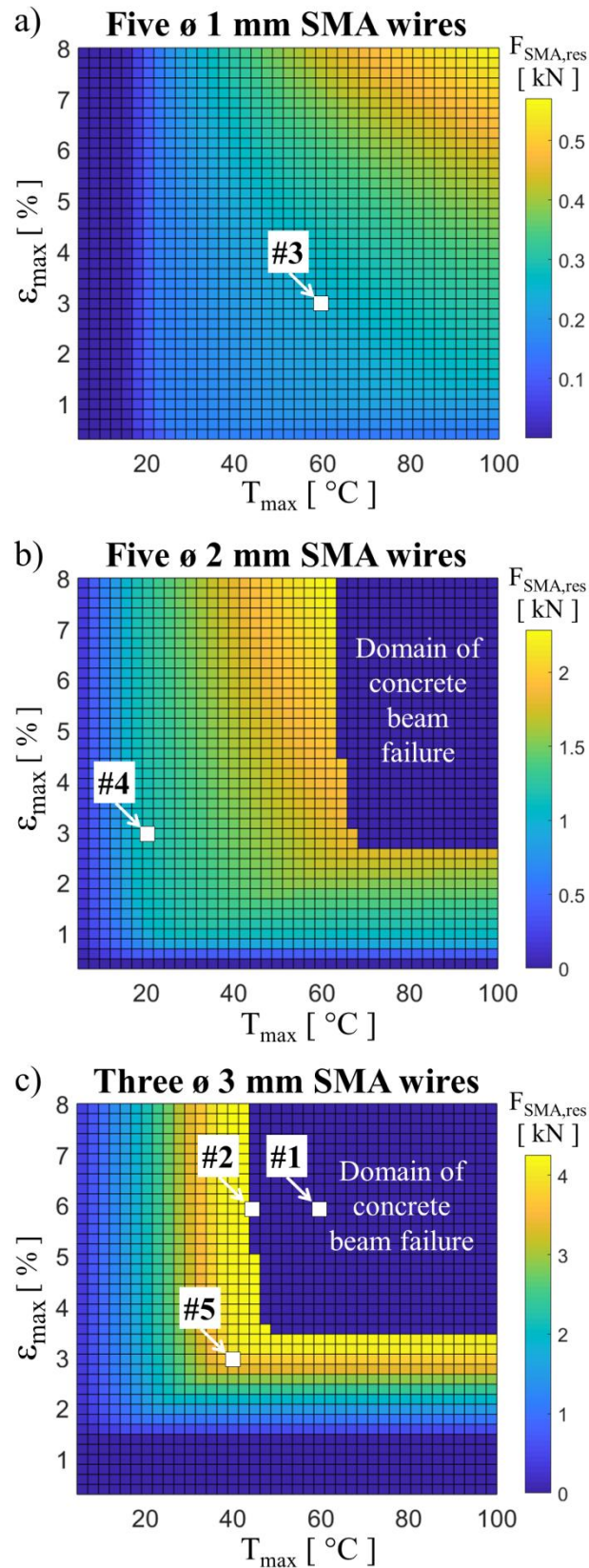


**Fig. 13** Simulation results: total force  $F_{SMA,res}$  in the SMA wires at end of the procedure (*i.e.* after cooling down to ambient temperature) as a function of the maximum temperature  $T_{max}$  and pre-strain  $\epsilon_{max}$  of the SMA wires. Locations corresponding to the experimental tests conditions #1 to #5 are also indicated in the maps.